



Dual-strategy-encapsulated phase change materials with thermal immune functions for efficient energy storage and all-climate battery thermal management

Gang Zhou^{a,1}, Ling Li^{a,1}, Seul-Yi Lee^{b,1}, Fei Zhang^c, Junwen Xie^c, Bin Ye^d, Wenhui Geng^d, Kuikui Xiao^d, Jong-Hoon Lee^b, Soo-Jin Park^{b,*}, Zhi Yang^{a,d,**}, Chengzhe Huang^{a,***}, Yinhang Zhang^{a,d,e,****}

^a College of Chemistry and Materials Engineering, Wenzhou University, Wenzhou, 325035, PR China

^b Department of Chemistry, Inha University, 100 Inharo, Incheon, 22212, South Korea

^c School of Science and Engineering, The Chinese University of Hong Kong, Shenzhen, 518172, Guangdong, People's Republic of China

^d Key Laboratory of Carbon Materials of Zhejiang Province, College of Chemistry and Materials Engineering, Wenzhou University, Wenzhou, 325035, China

^e Rui'an Graduate College of Wenzhou University, Wenzhou, Zhejiang, 325206, PR China

ARTICLE INFO

Keywords:

Phase change material
Thermal conductivity
Electrical conductivity
Electromagnetic interference
Thermal management

ABSTRACT

The utilization of phase-change materials (PCMs) has garnered great interest in purposes of energy storage and thermal management due to its lightweight, high-energy efficiency, and cost-competitiveness. However, the intrinsic limitations of low thermal conductivity and leakage in PCMs impede their usage in high-power-density energy harvesting applications. Here, we designed multifunctional phase-change composites (PCCs) via a dual-encapsulation strategy to realize all-climate thermal managements for lithium-ion batteries. For PCMs, polyethylene glycol was interpenetrated into porous polyurethane network (PEG@PU) to enclose a considerable amount of PEG. Then, the PCMs were infiltrated into the highly oriented graphite frameworks (HOGF). A series of processes enabled to form multi-layered structures as well as alleviate the leakage issue of PEG, and thereby improving the thermal storage ability. The so-obtained PCCs exhibited excellent electrothermal properties (134.9 °C at 1.8 V) and high electromagnetic interference performances (larger than 90 dB). These findings presented that the thermal managements of PCCs can be utilized as active preheating or passive cooling system in a battery thermal management system for the all-climate demands.

1. Introduction

Potential battery accidents have been one of the key factors restricting the increase of electric vehicle (EV) market penetration [1,2]. The occurrence of EV-related accidents is closely related to the failure of the thermal management system during the usage of EVs. Normally, high operating temperatures deteriorate battery cycle life and cause thermal runaway of the cell or the whole battery pack, resulting in accidents [3–5]. Low charging temperatures or low operating temperatures will reduce the capacity of power batteries and lead to side

reactions, thus inducing performance degradation [2,6–8]. Developing highly efficient thermal management materials for EV battery packs to ensure their operation within a reasonable temperature range has become an urgent and significant requirement [9–11].

Phase-change materials (PCM) have been developed as promising energy storage materials to address the problems of energy supply and demand [12–14]. Polyethylene glycol (PEG), a PCM, has attracted considerable interest due to its high latent heat of phase change, environment friendliness, low cost, and recyclability. However, leakage issues and intrinsically low thermal conductivity of PEG have greatly

* Corresponding author.

** Corresponding author. College of Chemistry and Materials Engineering, Wenzhou University, Wenzhou, 325035, PR China.

*** Corresponding author.

**** Corresponding author. College of Chemistry and Materials Engineering, Wenzhou University, Wenzhou, 325035, PR China.

E-mail addresses: sjpark@inha.ac.kr (S.-J. Park), yang201079@126.com (Z. Yang), 20160279@wzu.edu.cn (C. Huang), bank0719@163.com (Y. Zhang).

¹ Gang Zhou, Ling Li, and Seul-Yi Lee contributed equally to this work.

restricted its applications in the thermal management area [12,15–18].

Chemical grafting of PEG into supporting materials such as polyurethane to prepare solid-solid PCMs has been demonstrated as a feasible approach to address the leakage issue [19,20]. However, the newly formed bonding inside the PCM would greatly restrict the movement of the PEG molecules, thus resulting in decreased thermal energy storage capacity [21]. Another commonly used method to address the above issue is microencapsulation [22–24]. PEG can be encapsulated by polymers to form core-shell structures by in-situ polymerization, interfacial polymerization, suspension-like polymerization, and complex coacervation for leakage prevention [25,26]. However, although the anti-leakage effect is relatively significant, this technique is not widely adopted due to its complex preparation process and high cost. As a whole, the PEG based PCMs possess satisfied latent heat, but their leakage issues and low phase change temperature (usually below 55 °C) are still difficult to solve.

The intrinsically low thermal conductivity ($0.13\text{--}0.19\text{ Wm}^{-1}\text{K}^{-1}$) of PEG is another barrier limiting its commercial applications [27–29]. High thermal conductivity can promote the energy storage efficiency of the PCMs, thus realizing fast thermal response and improved working efficiency of the PCMs. Incorporating thermally conductive fillers into the PCMs can help in the preparation of high-thermal-conductivity phase-change composites (PCCs). However, the mechanical properties and heat-storage performance of PCCs are often compromised on account of the addition of a large amount of thermally conductive fillers [30–35]. In particular, a meticulously designed 3D thermal conductivity network in the PCCs is widely used to simultaneously generate high thermal conductivity and high energy storage [36]. However, PCCs based on 3D thermal conductive networks, such as aerogel, foams, and skeletons, mostly exhibit thermal conductivities below $5\text{ Wm}^{-1}\text{K}^{-1}$ [37, 38]. Therefore, it is challenging to develop PCCs with excellent thermal stability, high thermal conductivity, and large latent heat, simultaneously, for scalable thermal storage and battery thermal management applications.

Various of studies have been reported to prepare highly thermal conductive PCCs to realize the application of PCCs in battery thermal management. Wu et al. [39] fabricate highly conductive and liquid-free phase change composites for thermal management of battery by constructing a polyurethane/graphite nanoplatelets hybrid network via pressure-induced assembly. The prepared material is demonstrated for efficient battery thermal management toward versatile demands of active preheating and passive cooling. Deng et al. [40] prepared a multifunctional and flexible PCM with high anti-leakage and thermal conductivity performances. The maximum temperature of the battery module with multifunction flexible PCM can be controlled below 45 °C even at 1.5C discharge rate.

In this work, a multifunctional PCC with a versatile performance was ingeniously designed using a dual-encapsulation strategy, aimed at realizing the application of all-climate thermal management of lithium-ion batteries. Here, 3D network polyurethane (3D PU) was synthesized and physically mixed with the PEG molecular to ameliorate the leakage of the PEG and, simultaneously, enhance the thermal storage ability of PEG@PU due to the intrinsically high phase-change performance of PU. Thereafter, PEG@PU was filled into a highly oriented graphite framework (HOGF) using a vacuum infiltration approach to further alleviate the leakage issues of PEG. The prepared PEG@PU/HOGF composites exhibited excellent in-plane thermal conductivity of $36.52\text{ Wm}^{-1}\text{K}^{-1}$ and extremely low electrical resistance of $0.5\text{--}2\ \Omega$, thus realizing outstanding electrothermal ($134.9\text{ }^\circ\text{C}$ at 1.8 V) and high electromagnetic interference (EMI) performances ($\sim 90\text{ dB}$). The prepared PCC was demonstrated in a battery thermal management system for addressing all-climate demands by taking advantage of its active preheating and passive cooling abilities. This work provides a promising and feasible approach for the mass production of high-performance PCCs for energy storage and battery thermal management applications.

2. Experimental

2.1. Materials

Dibutyltin dilaurate (DBTDL, 95%); polyaryl polymethylene isocyanate (PAPI, average functionality is 3); N,N-dimethylformamide (DMF, 99.5%, AR); and PEG (AR, $M_n = 2000\text{ g mol}^{-1}$) were purchased from Shanghai Aladdin Biochemical Technology Co., Ltd, China. Graphite papers (GP, thickness: 3 mm) were purchased from Guangshengjia New Materials Co., Ltd, China. Sulfuric acid (H_2SO_4 , 98%) and nitric acid (HNO_3 , 63%) were purchased from Zhejiang Zhongxing Chemical Reagent Co., Ltd, China.

2.2. Fabrication of HOGF

H_2SO_4 and HNO_3 , with a constant volume ratio (1:1), were blended thoroughly in an ice bath under vigorous stirring for 20 min. To obtain the HOGF, GPs of different sizes were immersed in the acid mixture, and the expansion lasted for 1 h. The obtained HOGF was rinsed with water for 12 h until a neutral pH state was obtained. Finally, the HOGF was dried under $100\text{ }^\circ\text{C}$ in an oven for 12 h.

2.3. Fabrication of PEG@PU

The PCM, PEG@PU, was synthesized by a facile one-pot method, and the reaction process is shown in Figure S1 and Fig. 1a. First, 0.03 mol PEG was introduced into a 500 mL beaker at a heating temperature of $100\text{ }^\circ\text{C}$. Then, 150 mg DBTDL acting as a catalyst was added to the beaker and fully mixed with the melted PEG under gentle stirring. Further, 0.06 mol of PAPI was dissolved in 60 mL DMF and then dropped into the above solution. When the solution became viscous, a certain amount of PEG was added quickly into the solution under vigorous stirring. The 3D PU network absorbed the PEG molecules during this process, and subsequently, the solution was transferred into a vacuum oven at $80\text{ }^\circ\text{C}$ and dried for 12 h. Finally, the PEG@PU complex was obtained.

2.4. Fabrication of HOGF/PEG@PU composites

The whole fabrication process is shown in Fig. 1a. Through calculation, the HOGF was compressed to the proper thickness for the quantitative absorption of PEG@PU. The HOGFs with different thicknesses were added into sufficient PEG@PU solutions and then shifted to a vacuum oven with a preheated temperature of $80\text{ }^\circ\text{C}$. The PEG@PU was absorbed by the HOGF until no bubbles were observed. Subsequently, the oven was turned off, and the inside temperature was dropped naturally to room temperature. A block was obtained, and the redundant PEG@PU was removed by the blade. The obtained blocks were named as PCC $_x$, where x represents the HOGF content. For example, PCC $_{20}$ represents the HOGF content in the HOGF/PEG@PU composites of approximately 20 wt%. Then, two holes with cell diameters were drilled in the center of the PCC $_{20}$ block, and the cells were fitted tightly into the holes.

2.5. Characterization

The SEM images were recorded using Nova 200 NanoSEM at 10 kV to observe the morphologies of the fracture surface of the HOGF with different expansion rates. The XRD (D8ADVANCE, BRUKER) was employed to determine the crystalline structure of the GP and HOGF. The X-ray intensity was determined at a scanning rate of 20° min^{-1} with a 2θ from 10° to 75° . Renishaw inVia Raman spectrometer (Renishaw) equipped with an Ar-ion laser (532 nm) was used to detect the Raman signals of the GP and HOGF at room temperature. The FT-IR spectra of the PEG, PAPI, and synthesized 3D PU were obtained using Fourier-transform infrared spectroscopy (PerkinElmer, Frontier, USA).

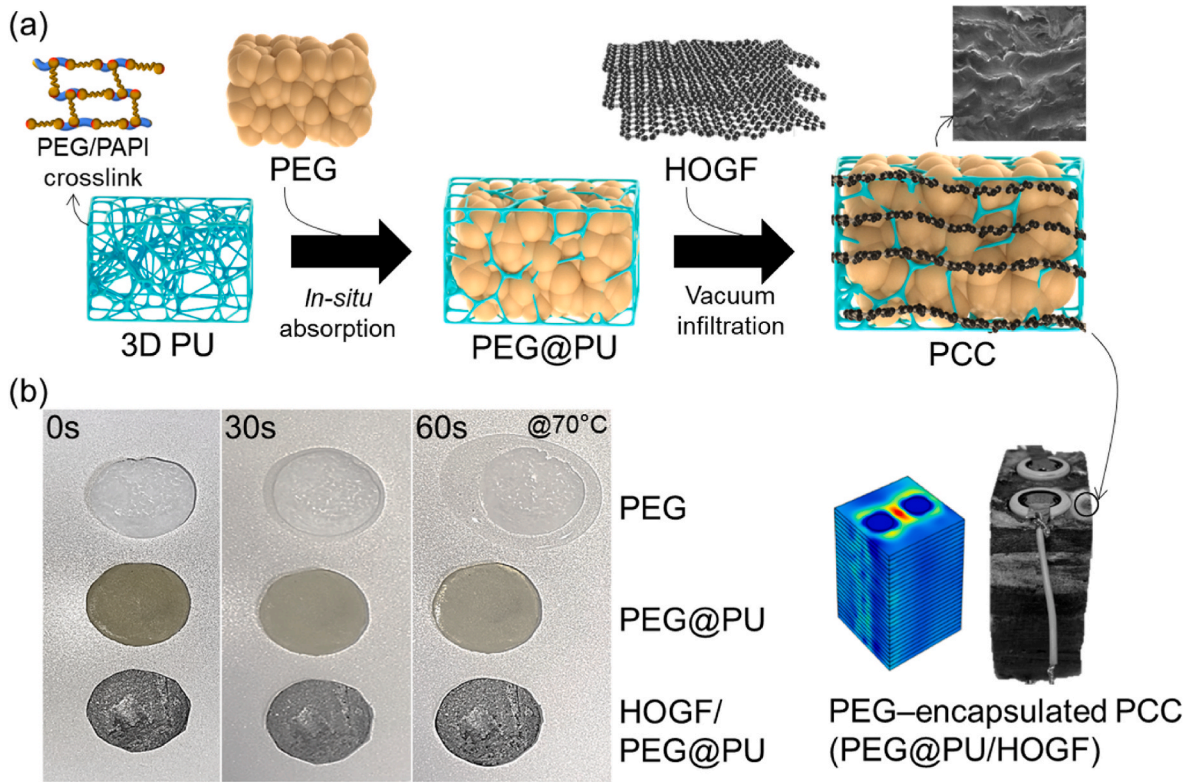


Fig. 1. The schematic illustration of (a) preparation of PCCs and (b) digital images of PEG, PEG@PU, and HOGF/PEG@PU heated at 70 °C for 0 s, 30 s, and 60 s.

The in-plane and through-plane thermal conductivities were calculated using the following Equation (1)

$$K = \alpha \rho C_p \quad (1)$$

where α is the thermal diffusivity, C_p is the specific heat capacity, and ρ is the density of samples. The value of α was determined by LFA 447 (Nanoflash). C_p was examined using METTLER DSC 3 (METTLER TOLEDO, Swiss). The ρ values of the samples were calculated by dividing the mass with the corresponding volumes. The samples were cut into discs of diameters 12.7 mm and 25.4 mm to measure the through-plane and in-plane thermal conductivities, respectively.

To verify the thermal conductive performance, a thermal imaging camera (FOTRIC, 224s) was used to record the surface temperature and temperature distributions on the samples. The photographs taken by this camera could be transformed into 3D infrared thermal images through image software packages (AnalyzeIR, FOTRIC). To implement the electrothermal performances of the samples, an M8813 150 V/1A Maynuo DC Source Meter was used to provide different voltages, and the varying temperature was collected by a Paperless Recorder (KSB1-24AOR, China) connected with a temperature infrared sensor (KS instrument, China). The electrothermal conversion efficiency was calculated using Equation (2)

$$\eta = \frac{m\Delta H}{UIt} \quad (2)$$

where m represents the weight of the sample; ΔH is the phase change enthalpy; U and I are the applied voltage and corresponding current during testing, respectively; t is the duration of the phase transition.

To verify the feasibility of the prepared PCCs in the battery thermal management, commercial 18650 lithium-ion cells were adopted. All the characterizations for either the PCC-wrapped or naked cells were conducted under the same environment. In the preheating process, the external voltage was applied to the two sides of the composite block to implement the preheating of the cells. The surface temperature of the

cell during both the preheating and cooling tests was monitored by an RTD temperature sensor (PT100) stuck on the battery surface.

A vector network analyzer (CETC, AV36290) was employed to evaluate the EMI shielding efficiency of the PCCs in the X band (8.2–12.4 GHz). The reflection coefficient (R), the transition coefficient (T), the absorption coefficient (A), SE reflection (SE_R), SE absorption (SE_A) and the SE total (SE_T) could be calculated through the below equations:

$$R = |S_{11}|^2 \quad (3)$$

$$T = |S_{21}|^2 \quad (4)$$

$$A = 1 - R - T \quad (5)$$

$$SE_R(dB) = -10 \times \log(1 - R) \quad (6)$$

$$SE_A(dB) = -10 \times \log\left(\frac{T}{1 - R}\right) \quad (7)$$

$$SE_T(dB) = -10 \times \log(T) = SE_R + SE_A \quad (8)$$

3. Results and discussion

Unlike normal linear PU, here, a 3D network PU was synthesized, taking advantage of the unique three isocyanate groups (Fig. S1) in one molecule of PAPI. The purpose of this unique design is to wrap the PEG molecules like a net, thus effectively preventing their leakage. The synthesized PEG@PU was then infiltrated into the HOGF, as shown in Fig. 1a. The layer structures were not destroyed during the vacuum infiltration process. The oriented graphite layers could further ameliorate the leakage issue of the PEG molecules at high temperatures. The leakage experiment was conducted for the PEG, PEG@PU, and HOGF/PEG@PU, and the results are shown in Fig. 1b. It can be seen that under 70 °C, the PEG melts very fast, while no distinct melting signs were

observed for PEG@PU and HOGF/PEG@PU, demonstrating the effectiveness of this dual-encapsulation strategy.

The characterization results of the HOGF are shown in Fig. 2. As shown in Fig. 2a and b, after the acid treatment, the thickness of the HOGF reached 13 mm, which is 4.3 times thicker than that of pristine GP, whose initial thickness was 3 mm. Although it expanded significantly in the thickness direction, it remained unchanged in the horizontal. The layer structures and holes result in a low density of 273.8 mg cm^{-3} . Its light weight was also demonstrated by placing it steadily on a grass blade, as shown in Fig. 2c. Fig. 2d shows that the expansion rate increased with the increasing acid treatment time. Moreover, the expansion rate could be easily adjusted by compressing the fully expanded HOGF to its target values, as shown in Fig. S3. Because of the facile preparation approach, the HOGF can be easily realized in mass production either in the laboratory or in an enterprise. The morphologies of the graphite paper and HOGF with different expansion rates are

shown in Fig. 2e–g. The graphite paper exhibited a densely packed structure, while the HOGF exhibited a loose and layered structure, and the interlayer distance increased at a larger expansion rate. Whether macroscopic (Fig. 2c and d) or microscopic (Fig. 2e–g), the oriented structure of the graphite layer can be clearly seen. With the increased expansion rate, the orientation degree decreased. This may be attributed to the expansion force that caused the distortion of graphite layers. However, this expansion force did not destroy the integrity of the graphite layers. The layer structure is better for the infiltration of PEG@PU into the HOGF compared pore structures to form more stable structure. X-ray diffraction (XRD) was then carried out to determine the crystalline defects caused by the acid treatment (Fig. 2h). Surprisingly, after the acid treatment and expansion, the intensity of the 002 peak became stronger, demonstrating a better crystalline structure of the HOGF. This anomaly was further verified by the Raman results shown in Fig. 2i. A D peak was clearly observed on graphite paper; however, it

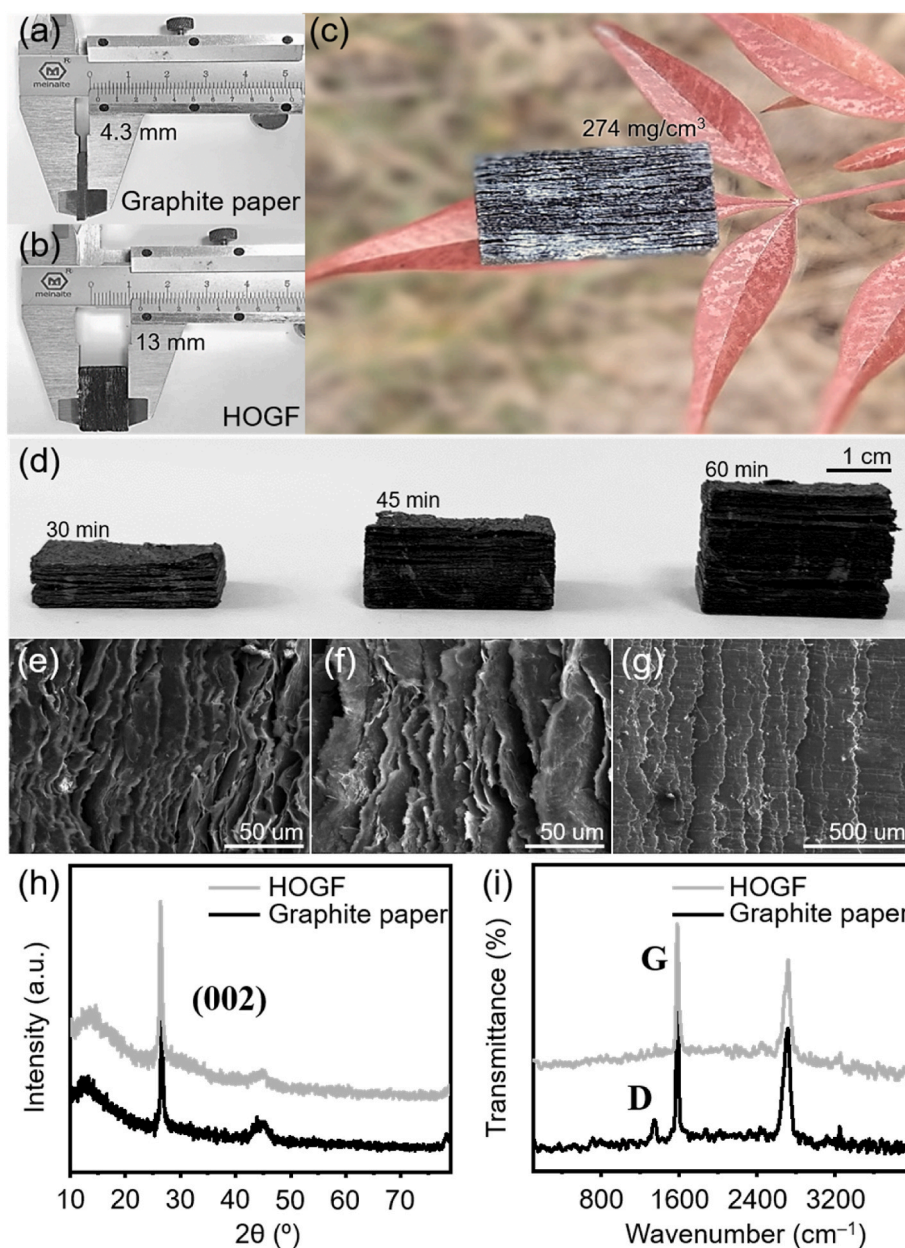


Fig. 2. The thickness of the GP (a) before and (b) after expansion; (c) The light HOGF could stand stably on the surface of grass; (d) optical images of HOGF with different expansion; (e–g) The morphology of fracture surface of HOGF with different expansion rate; (h) The XRD patterns of the graphite paper and HOGF; (i) The Raman results of the graphite paper and HOGF rate.

vanished in the HOGF. We inferred that the low-temperature acid treatment washed away the magazines on the surface of the graphite layer but did not destroy the graphite crystallinity and its integrated microstructure.

The FT-IR was employed to demonstrate the successful synthesis of PU, and the related spectra of PAPI, PEG, and synthesized PU are presented in Fig. S4. In the PAPI molecules, a peak detected at 2260 cm^{-1} corresponds to the $-\text{NCO}$ groups. In the case of PEG, a strong absorption peak appearing at 2880 cm^{-1} corresponds to the C-H stretch. The peaks appearing at approximately 3423 cm^{-1} can be ascribed to the $-\text{OH}$

stretching vibration. After the reaction, the $-\text{NCO}$ groups at 2260 cm^{-1} in the spectrum of PU disappeared, while the new stretching vibration peaks of $-\text{NHCOO}-$ at 1726 and 1537 cm^{-1} formed by the polymerization of PEG and PAPI emerged, thus verifying the successful synthesis of PU.

Except for the leakage issue, thermal conductivity is another key factor affecting the energy storage efficiency and temperature control ability of the PCMs. Herein, a HOGF structure was assigned to be a thermally conductive medium, mainly due to its light weight, low cost, ease of mass production, and highly aligned layer structures, making it a

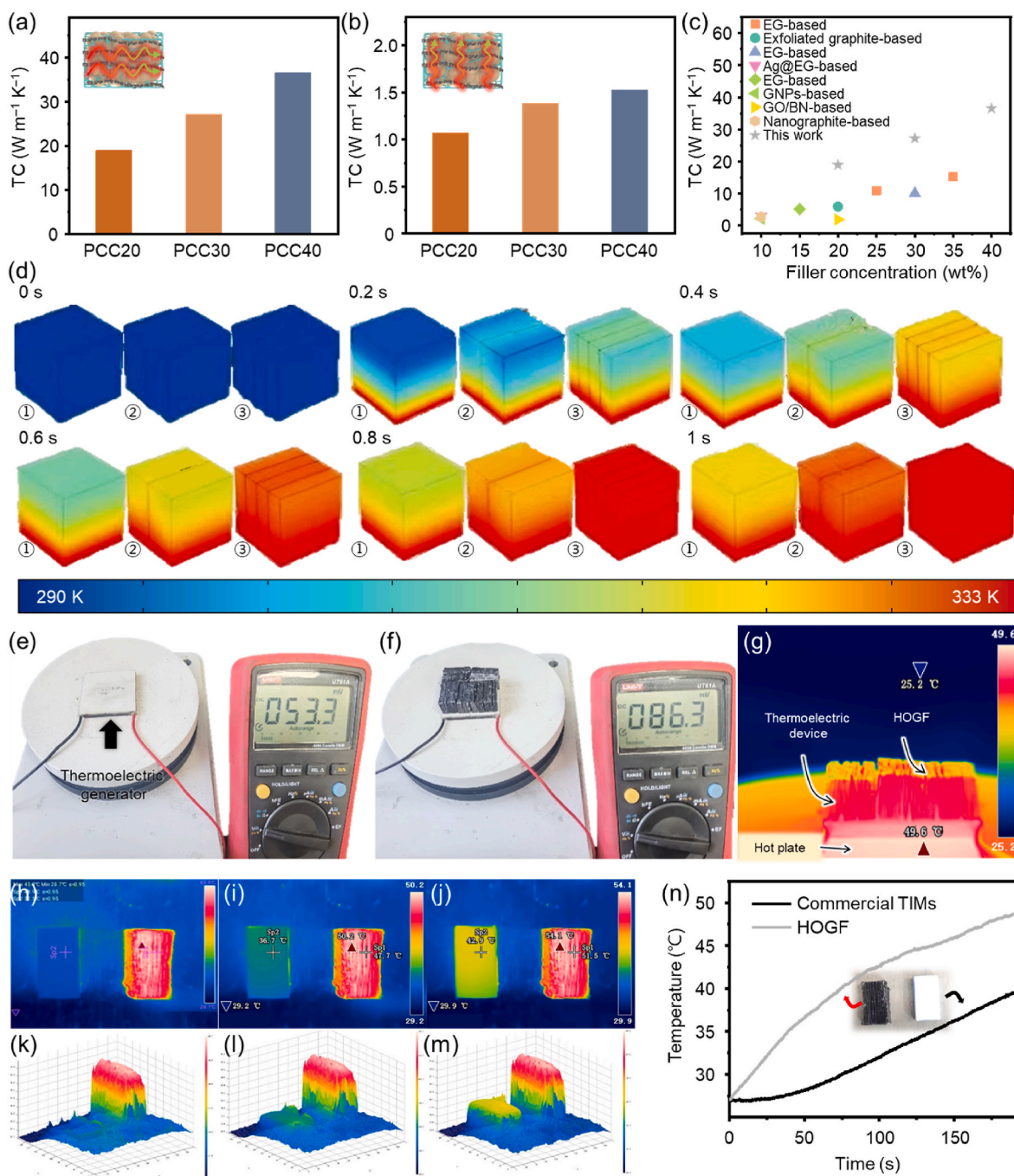


Fig. 3. The (a) in-plane and (b) through plane thermal conductivity of PCCs; (c) A comparison of thermal conductivity of the PCCs with those reported in other literature; (d) Finite element analysis of heat transfer in pure PEG@PU (①), and PCCs(② and ③); (e) A thermoelectric generator as a contrast heated at $50\text{ }^{\circ}\text{C}$; (f) A thermoelectric generator heated with $50\text{ }^{\circ}\text{C}$ using PCC as heat sink; (g) An infrared image of the thermoelectric generator when working; (h–j) The infrared images of commercial conductive silicon pad (left) and HOGF (right) heated at $60\text{ }^{\circ}\text{C}$ with different heating time; (k–m) The corresponding 3D infrared images of the figures shown in h, i, and j, respectively; (n) Time-dependent surface temperatures of the commercial conductive pad and HOGF heated at $60\text{ }^{\circ}\text{C}$.

potential material for thermal conduction. The in-plane and through-plane thermal conductivities of the PCCs were determined, and the results are presented in Fig. 3a and b. It can be observed that with the increasing HOGF loading, both in-plane and through-plane thermal conductivities increased. The in-plane thermal conductivity reached $36.52 \text{ W m}^{-1}\text{K}^{-1}$ at an HOGF loading of 40%, outperforming the many results reported in other literature (Fig. 3c) [41–48]. It is clear that a higher thermal conductivity can be achieved with a further increase in the HOGF concentration. The high in-plane thermal conductivity can be attributed to the highly oriented graphite layers, which can act as a highway for phonon transferring (Fig. S2), thus realizing fast heat transportation [49,50]. The through-plane thermal conductivity of the prepared composites only reached $1.53 \text{ W m}^{-1}\text{K}^{-1}$ at the 40% HOGF loading, mainly because of the phonon scattering among graphite layers and the lack of effective heat transport tunnels in the vertical direction.

A COMSOL Multiphysics® simulation software was employed to conduct finite element simulation to model the heat flow and temperature distribution during the heating process in pure PEG@PU and its composites. A transient-state finite element method was used to model the heat flow and temperature distribution. The outer boundaries were recognized as thermal insulators with an initial temperature of $20 \text{ }^\circ\text{C}$, and the bottom side of the samples was set to be $60 \text{ }^\circ\text{C}$. As shown in Fig. 3d, the heat diffused slowly in pure PEG@PU (model ①) because of excessive phonon scattering in the polymers and lack of a heat conduction path, while in the HOGF-incorporated composites (model ② and ③), with the increasing HOGF concentration, the heat diffused faster from the bottom toward the top of the samples, thereby demonstrating the excellent thermal conductive ability of the HOGF.

The latent heat of the three samples were determined using DCS to judge their heat storage density, and the results are presented in Fig. S5a. As expected, with the increased HOGF content, the latent heat decreased from 106.59 J/g to 83.55 J/g . A comparison of thermal conductivity and latent heat storage density of PCCs from the literature was shown in Fig. S5b. It is well known that a larger filler content (a higher thermal conductivity), a lower latent heat will be for the PCCs. Although the latent heat of our samples is not as high as the values reported by other studies [51–55], but our samples exhibited a much higher thermal conductivity, which could accelerate the heat absorption efficiency.

A thermoelectric generator was utilized to verify the heat dissipation capacity of the HOGF. It is known that with a larger temperature difference between two sides of a thermoelectric generator, more electricity and larger voltages can be generated. As shown in Fig. 3e and f, the bottom side of the thermoelectric generator was heated to $50 \text{ }^\circ\text{C}$, and the generated voltage for the thermoelectric generator without any heat sink (Fig. 3e) reached 53.3 mV . In contrast, for the one using the HOGF as a heat sink (Fig. 3f), the generated voltage reached 86.3 mV , thereby demonstrating the superior heat dissipation capacity of the HOGF. An infrared image for the HOGF-configured thermoelectric generator was then obtained (Fig. 3g), and it was observed that heat could be promptly transferred from the upper side of the thermoelectric generator to the HOGF, thus increasing the temperature difference and resulting in a higher output voltage.

For further demonstrating the high heat dissipation capacity of the prepared composites, a commercial thermally conductive silicone pad with a thermal conductivity of $3 \text{ W m}^{-1}\text{K}^{-1}$ was employed as a reference material. The silicone pad, with a thickness of 5 mm , was placed on a hotplate, and then a HOGF of the same size was placed on its right side. Both samples were heated at $60 \text{ }^\circ\text{C}$, and an infrared camera was used to take the heat distribution images. The related images and the temperature variation curves are presented in Fig. 3h–k. It can be seen that the surface temperature of the HOGF increased much faster than that of the commercial silicone pad. The surface temperature of the HOGF reached $37.91 \text{ }^\circ\text{C}$ after 60 s while that of the silicone pad only reached $28.78 \text{ }^\circ\text{C}$ after the same amount of time. The heat distribution can be more intuitively reflected by a 3D heat distribution map shown in Fig. 3l–n.

The temperature for the HOGF was much higher for the whole time than that of the commercial silicone pad, and the heat was evenly distributed on the surface of the HOGF. This phenomenon indicates that the prepared material has better heat transfer ability.

It is well known that high electrical conductivity is a key factor dominating the Joule heating effect of electrothermal materials. In this work, the integrated and continuous graphite structure endows the HOGF with excellent electrical conductivity, thus resulting in satisfactory electrothermal efficiency and low energy cost. Based on the electrothermal conversion, the as-prepared HOGF was selected as an electrical heater to study its electrothermal performance. The related results are presented in Fig. 4a–e. The time-dependent surface temperatures under various output voltages are plotted in Fig. 4a. It appeared that surface temperature increases rapidly after applying an external voltage. The saturated surface temperature enhanced with the increasing output voltage, and with an external voltage of only 1.8 V , the saturated surface temperature reached $134.9 \text{ }^\circ\text{C}$ with a current of 8.35 A . Owing to the high saturation temperature at a low voltage and the short thermal response time, the HOGF may find potential applications in various thermal devices. Moreover, the heating temperature of the prepared HOGF could be rapidly adjusted in real-time after regulating the applied external voltages from 0.3 to 1.8 V or from 1.8 to 0.3 V (Fig. 4b), thereby demonstrating the fast thermal response and efficient electric-to-heat conversion under different voltages. Then, cyclic heating and cooling of the HOGF were performed under an output voltage of 1.5 V , and the results are shown in Fig. 4c. The HOGF showed a steady electrothermal performance after 20 power on-off cycles. The Joule heating performances of the HOGF were compared with the results reported in the previous studies [56–60] (Fig. 4e). The HOGF exhibited unique advantages, particularly under low voltages, outperforming most other electric heaters. A thermodynamic analysis for the HOGF was then conducted during the working process for the in-depth investigation of the heating mechanism. The following equation can calculate the saturation temperature (T_s) of the heater surface:

$$T_s = T_0 + \frac{U^2}{RhA} \quad (3)$$

where T_0 is the ambient temperature, U is the output voltage, R is the heater resistance, h is the coefficient of convective heat transfer, and A is the heating area of the heater. The data used for this equation were the values extracted from Fig. 4a. It can be seen in Fig. 4d that a linear fitting of T_s versus U^2 through Equation (3) was obtained, and T_s exhibited a linear relation with U^2 , thereby demonstrating the precision of the theoretical prediction of T_s under various applied voltages [61].

The electrothermal performances of PCC20 were then conducted, and the related results are presented in Fig. 4g. It can be noted that the morphologies of the heating and cooling curves of PCC20 are distinctively different from those of the HOGF. The temperature rapidly increased to approximately $50 \text{ }^\circ\text{C}$ at an initial stage, and then the speed decreased with a small slope. The reason for this phenomenon can be ascribed to the absorption and storage of the latent heat produced by the HOGF network by the PCMs. After the energy storage stage, the temperature started to increase again rapidly. Moreover, it can be observed that with the enhanced external voltages, the phase-change time is shortened, thereby demonstrating a fast energy-storage capacity of the prepared PCCs. The temperature distribution recorded by an infrared camera is shown in Fig. 4h. It is well known that maintaining the temperature homogeneity in a battery pack is of paramount importance for its safe operation. The related 3D infrared thermal images were transformed using an image software package (AnalyzeIR, FOTRIC). During the working process, the generated heat was evenly distributed on the heater surface, thereby demonstrating its uniform heating ability. The electrothermal conversion efficiency of PCC20 was then calculated, and the results are shown in Fig. 4f. When the applied voltages increased to 1.7 V , the efficiency reached a maximum of 80.17% . The high energy

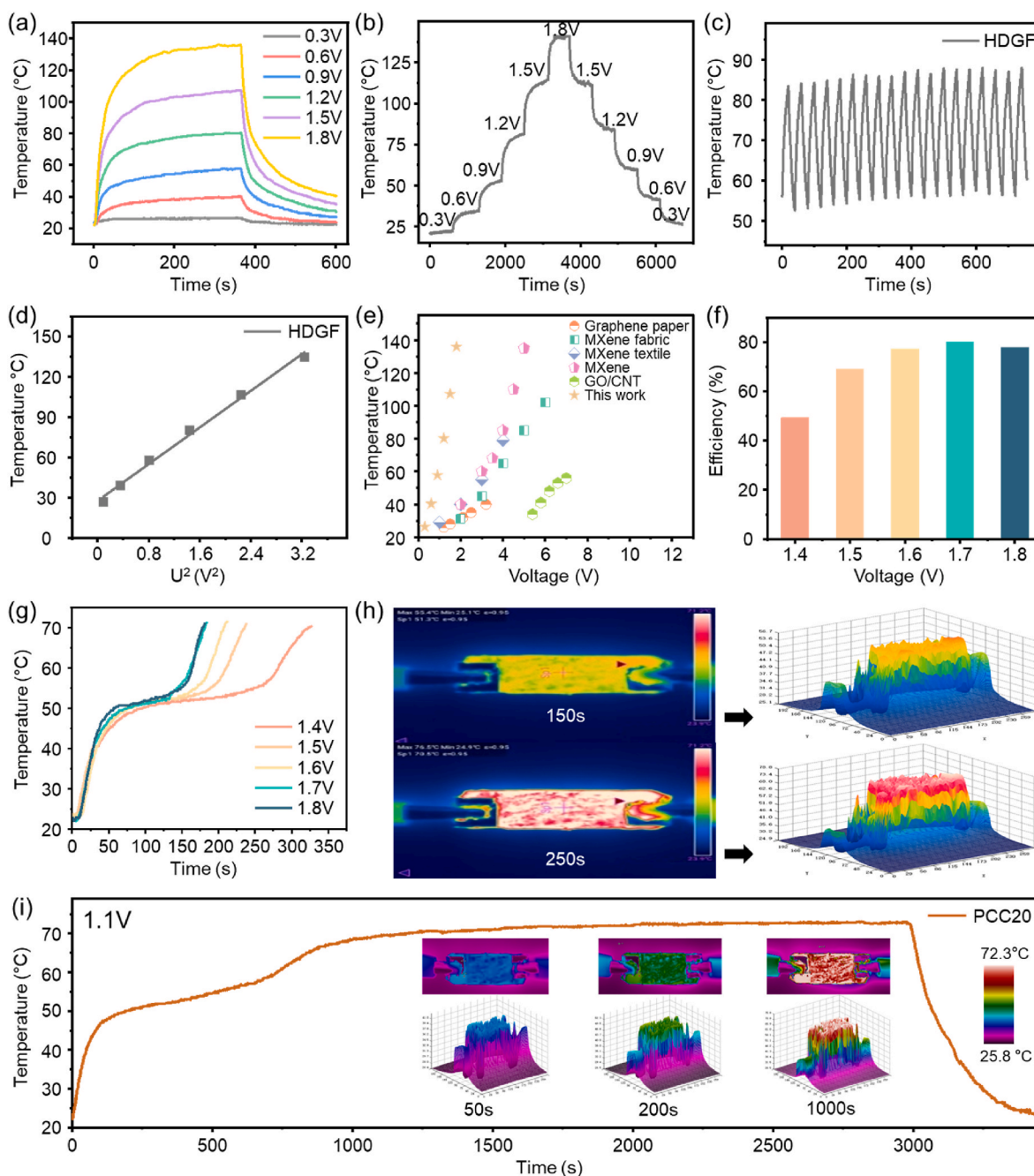


Fig. 4. (a) Time-dependent surface temperature variations of the HOGF with different applied voltages; (b) surface temperature variations of HOGF vs voltages; (c) cyclic heating test of the HOGF under supplied voltage of 1.5 V; (d) experimental results and corresponding linear fitting of saturated temperature versus U^2 ; (e) A comparison result of Joule heating performances with those reported in other literature; (f) Electrothermal conversion efficiencies of the PCC20 under different voltages; (g) Time-temperature evolution curves of the PCC20 under different voltages; (h) The corresponding 2D and 3D infrared images of PCC20 under external voltage of 1.4 V at 150 and 250 s; (i) Long-term heating test under 1.1 V, the inset are the corresponding 2D and 3D infrared images of PCC20 at different working time.

conversion efficiencies at high voltages could be ascribed to the low phase-change time at higher voltages, which suppressed the heat loss through convection and radiation to the surrounding environment [21]. Finally, the heater was heated to 73 °C and maintained at that temperature for a long duration of 3000 s (Fig. 4i). The saturation temperature of this device was kept stable, thereby demonstrating a long-term stable electrothermal performance. The infrared images and the related 3D infrared thermal images at the different working times are presented in Fig. 4i, and it can be seen the sample was heated up evenly.

The battery pack of the newer energy vehicle consists of hundreds or thousands of cells, and each of them emit electromagnetic waves to the

outside surroundings [62,63]. Here, the EMI shielding performances of the PCCs were evaluated in the range of 8.2–12.4 GHz, and the results are shown in Fig. 5a. It can be seen the EMI shielding effectiveness (SE) enhanced with the increasing HOGF concentration. The SE reached 35 dB for the sample PCC20 and 95.2 dB for the sample PCC40, which can be attributed to their higher-density conductive networks. All the SE values of the PCCs far exceeded the civil standard (20 dB) for shielding electromagnetic radiation [64]. The S-parameters—A, R, and T—are presented in Fig. 5b. It can be seen that R is always larger than A for all PCCs, thereby indicating that the reflection is dominant for EMI. Meanwhile, the value of T (in inset) was reduced to 0 for PCC30 and

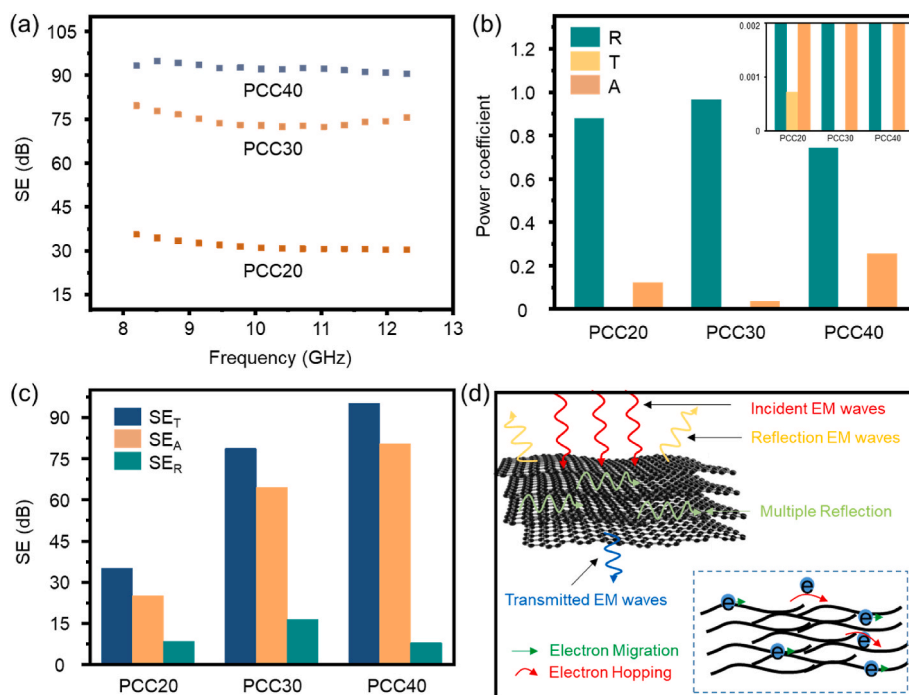


Fig. 5. (a) EMI SE of the PCCs; (b) Average R, T, and A of the PCCs; (c) Average SE_R and SE_A of PCCs; (d) Schematic illustrations for the EMI shielding mechanism of PCCs.

PCC40, indicating that almost all electromagnetic waves were shielded by the HOGF. To further explore the EMI shielding performance, SE_R, SE_A, and SE_T over the whole X band are presented in Fig. 5c. For all samples, SE_A was much larger than SE_R, indicating that the absorption efficiency of microwaves is larger than the reflection efficiency for the absorbed microwaves. A schematic illustration of the possible underlying shielding mechanism is provided in Fig. 5d. When the electromagnetic waves came in contact with the PCCs, a large fraction of incident electromagnetic waves were reflected immediately due to the

impedance mismatch between the air and PCC surface where large numbers of free electrons were distributed. Long-range ordered graphite layers could facilitate the transport of electrons, which in turn accelerated the consumption of electromagnetic waves. Most of the incident electromagnetic waves would be transferred to heat energy through multiple reflections among the hierarchical structures of the graphite layers.

We then demonstrated the thermal immune functions of the PCCs for the all-climate usage by employing the superior energy storage and

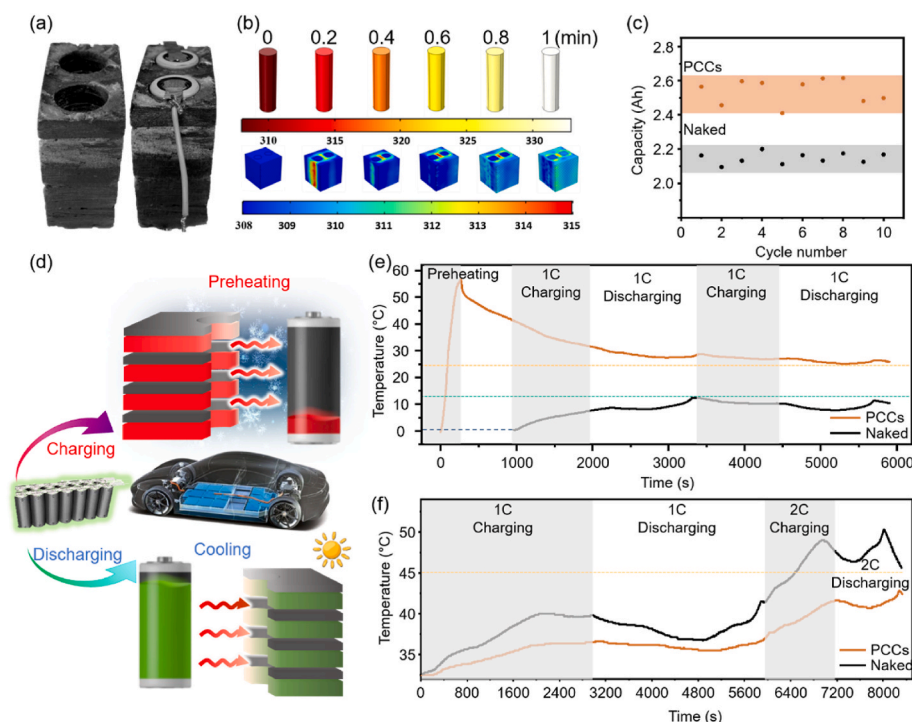


Fig. 6. (a) The digital image of the cell pack wrapped with PCCs; (b) Finite element analysis of heat transfer in naked cell and PCC wrapped cell; (c) Capacities of cell packs with and without PCC wrapping and preheating; (d) The thermal immune mechanism of prepared PCCs in battery thermal management; (e) Time-dependent temperature curves of the cell packs with and without PCC wrapping and preheating during charging and discharging at low temperature; (f) Time-dependent temperature curves of the cell packs with and without PCC wrapping during charging and discharging at 30 °C.

electrothermal conversion capabilities of the PCCs. A high-power-density temperature-controlled device prepared using a PCC20 block to regulate the operating temperature of a commercial 18650 lithium-ion battery was developed, and its digital image is shown in Fig. 6a. The characterizations for the battery thermal management for this device are referred to in the published work [21], and the thermal immune mechanism is presented in Fig. 6d. The active preheating system based on the Joule heating performance of the PCCs can be launched in a cold environment to warm up the battery pack before charging or discharging. In a high-temperature environment, the heat generated by the battery pack will be absorbed by the PCCs in the form of latent heat to carry out the passive cooling process. The synergistic effect of the active heating and passive cooling systems will always maintain an optimum working temperature range, thus preventing capacity loss and thermal runaway of the battery pack [21].

To verify the feasibility of this conception, two 18650 lithium-ion battery packs with and without the PCC20 wrapping were tested in a cold environment. The related temperature evolution curves for both the battery packs are shown in Fig. 6e. In the initial stage, an external voltage was used to drive the electrothermal conversion and preheat the wrapped battery pack before beginning the battery charging and discharging. The PCC-wrapped battery pack was preheated to approximately 40 °C, followed by initiating the battery charge and discharge process. It can be seen that the temperature of the PCC-wrapped samples was maintained at approximately 25 °C, while the bare battery pack suffered from a low working temperature of 0–10 °C under 1 C charging/discharging conditions. These results indicate that the positive preheating provided by releasing the latent heat of the PCCs could effectively ameliorate the operating temperature of the battery pack. It has been reported that preheating a lithium-ion battery pack at the charging stage, particularly from a cold start, can distinctly enhance its rate capability and cycle life [21,65,66]. This was also demonstrated in our studies. As shown in Fig. 6c, the PCC-wrapped battery packs exhibited a larger charge capacity of 2.4–2.6 Ah compared to those of the bare ones (2.1–2.2 Ah) at a low working temperature.

Then, a passive cooling performance driven by the phase transition of the PCC was also conducted. The charging and discharging of the battery pack with and without the wrapped PCCs were performed at an initial temperature of approximately 33 °C. The temperature evolution trends for both the battery packs are presented in Fig. 6f. It can be seen that the surface temperature of the PCC-wrapped battery is always lower than that of the one not wrapped during the whole process. For example, under a 2C discharge process, the temperature of the bare battery reached a maximum of 50.5 °C, while the temperature of the wrapped one was maintained within 42 °C, almost 8 °C lower. Then, the infrared images were obtained for both battery packs, which are shown in Fig. S6. It can be clearly seen that the surface temperature of the PCCs during the charging and discharging was much lower than that of the naked battery, thereby indicating the superior thermal management ability of the PCC. For a better understanding of the thermal management mechanism of the PCCs, the finite element analysis of heat transfer in a naked cell and a PCC-wrapped cell was performed, and the results are shown in Fig. 6b. The working temperature for both battery packs was 35 °C. Given the same working power, after 1 min, the surface temperature of the naked cell reached 60 °C, while that of the PCC-wrapped one only reached 42 °C. One more interesting thing is that at 0.2 min, hotspots could be clearly observed for the PCC-wrapped cells, but soon they disappeared due to the excellent thermal conductivity of the HOGF, which diffused the heat to the attached PEG@PU in a short time. This can effectively prevent the occurrence of local hot spots inside the battery to ensure that the battery works in a safe environment.

4. Conclusions

In summary, an expanded graphite block was prepared with highly oriented layer structures due to the liquid phase expansion of the

commercial graphite paper. Further, 3D network PU was synthesized and used for the PEG encapsulation to prevent PEG leakage. Then, PEG@PU was infiltrated into the HOGF to construct multifunctional PCCs used for battery thermal management. The highly oriented graphite layers not only enhanced the thermal conductivity of the PCCs (a maximum of 35 W m⁻¹K⁻¹) but also further alleviated the PEG leakage issue through a second encapsulation. The prepared PCCs also showed high EMI shielding ability, superior electrothermal performances, and an efficient electrothermal conversion efficiency. In the end, the thermal immune function of the prepared PCCs for the all-climate applications was demonstrated based on the excellent electrothermal performance and high thermal conductivity of the PCCs. The operating temperature of the battery was maintained in a moderate range, either in a cold or hot environment, which could guarantee the battery capacity and prevent the phenomenon of thermal runaway. This work provides a promising and feasible route for the mass production of high-performance PCCs for energy storage and battery thermal management for all-climate demands.

CRedit authorship contribution statement

Gang Zhou: Conceptualization, Methodology, Investigation, Writing original draft, Writing - review & editing. **Ling Li:** Conceptualization, Methodology, Investigation, Writing original draft, Writing - review & editing. **Seul-Yi Lee:** Methodology, Formal analysis, Investigation, Writing original draft, Writing - review & editing. **Fei Zhang:** Conceptualization, Methodology, Formal analysis, Investigation. **Junwen Xie:** Methodology, Formal analysis, Investigation, Writing original draft. **Bin Ye:** Formal analysis, Investigation, Validation. **Wenhui Geng:** Formal analysis, Investigation, Validation. **Kuikui Xiao:** Formal analysis, Investigation. **Jong-Hoon Lee:** Validation, Writing original draft. **Soo-Jin Park:** Supervision, Writing - review & editing. **Zhi Yang:** Supervision, Writing - review & editing. **Chengzhe Huang:** Supervision, Writing - review & editing. **Yinhang Zhang:** Supervision, Writing original draft, Writing - review & editing.

Declaration of competing interest

The authors declare that they have no known competing financial interests or personal relationships that could have appeared to influence the work reported in this paper.

Data availability

Data will be made available on request.

Acknowledgments

This research was supported by the National Natural Science Foundation of China (Grant No. 52302045,52203103), the Basic Scientific Research Projects of Wenzhou City (Grant No. G20220018), Zhejiang Xinmiao Talents Program (Grant No. 2023R451024), the National Research Foundation of Korea (NRF) grant funded by the Korea government (MSIT) (No. 2022M3J7A1062940 and 2023R1A2C1004109). This work was also supported by the Technology Innovation Program (or Industrial Strategic Technology Development Program-Development of technology on materials and components) (20010106, Adhesives with low water permeability and low outgassing) funded by the Ministry of Trade, Industry & Energy (MOTIE, Korea)

Appendix A. Supplementary data

Supplementary data to this article can be found online at <https://doi.org/10.1016/j.compscitech.2023.110256>.

References

- [1] X.G. Yang, T. Liu, C.Y. Wang, Thermally modulated lithium iron phosphate batteries for mass-market electric vehicles, *Nat. Energy* 6 (2) (2021) 176–185, <https://doi.org/10.1038/s41560-020-00757-7>.
- [2] J. Luo, D.Q. Zou, Y.S. Wang, S. Wang, L. Huang, Battery thermal management systems (BTMS) based on phase change material (PCM): a comprehensive review, *Chem. Eng. J.* 430 (2022), 132741, <https://doi.org/10.1016/j.cej.2021.132741>.
- [3] X.N. Feng, D.S. Ren, X.M. He, M.G. Ouyang, Mitigating thermal runaway of lithium-ion batteries, *Joule* 4 (4) (2020) 743–770, <https://doi.org/10.1016/j.joule.2020.02.010>.
- [4] X.N. Feng, M.G. Ouyang, X. Liu, L.G. Lu, Y. Xia, X.M. He, Thermal runaway mechanism of lithium ion battery for electric vehicles: a review, *Energy Storage Mater.* 10 (2018) 246–267, <https://doi.org/10.1016/j.ensm.2017.05.013>.
- [5] M.S. Kim, B.H. Lee, J.H. Park, H.S. Lee, W.H. Antink, E. Jung, J. Kim, T.Y. Yoo, C. W. Lee, C.Y. Ahn, S.M. Kang, J. Bok, W. Ko, X. Wang, S.P. Cho, S.H. Yu, T. Hyeon, Y.E. Sung, Operando identification of the chemical and structural origin of Li-ion battery aging at near-ambient temperature, *J. Am. Chem. Soc.* 142 (31) (2020) 13406–13414, <https://doi.org/10.1021/jacs.0c02203>.
- [6] M.T.F. Rodrigues, G. Babu, H. Gullapalli, K. Kalaga, F.N. Sayed, K. Kato, J. Joyner, P.M. Ajayan, A materials perspective on Li-ion batteries at extreme temperatures, *Nat. Energy* 2 (8) (2017), 17108, <https://doi.org/10.1038/nenergy.2017.108>.
- [7] S. Ma, M.D. Jiang, P. Tao, C.Y. Song, J.B. Wu, J. Wang, T. Deng, W. Shang, Temperature effect and thermal impact in lithium-ion batteries: a review, *Prog. Nat. Sci.-Mater.* 28 (6) (2018) 653–666, <https://doi.org/10.1016/j.pnsc.2018.11.002>.
- [8] S.H. Kim, J.H. Lee, J.W. Kim, S.Y. Lee, S.J. Park, Interfacial behaviors of basalt fiber-reinforced polymeric composites: a short review, *Adv. Fiber Mater.* 4 (2022) 1414–1433, <https://doi.org/10.1007/s42765-022-00204-0>.
- [9] A.G. Mohammed, K.E. Elfeky, Q.W. Wang, Recent advancement and enhanced battery performance using phase change materials based hybrid battery thermal management for electric vehicles, *Renew. Sustain. Energy Rev.* 154 (2022), 111759, <https://doi.org/10.1016/j.rser.2021.111759>.
- [10] G. Zhao, X.L. Wang, M. Negnevitsky, H.Y. Zhang, A review of air-cooling battery thermal management systems for electric and hybrid electric vehicles, *J. Power Sources* 501 (2021), 230001, <https://doi.org/10.1016/j.jpowsour.2021.230001>.
- [11] W.F. Wu, G.H. Ye, G.Q. Zhang, X.Q. Yang, Composite phase change material with room-temperature-flexibility for battery thermal management, *Chem. Eng. J.* 428 (2022), 131116, <https://doi.org/10.1016/j.cej.2021.131116>.
- [12] W. Lee, M. Seo, J. Kim, Ultra-high thermal conductivity and mechanical properties of a paraffin composite as a thermal conductive phase change materials for novel heat management, *Compos. Sci. Technol.* 220 (2022), 109282, <https://doi.org/10.1016/j.compscitech.2022.109282>.
- [13] J.Y. Zhang, D. Shao, L.Q. Jiang, G.Q. Zhang, H.W. Wu, R. Day, W.Z. Jiang, Advanced thermal management system driven by phase change materials for power lithium-ion batteries: a review, *Renew. Sustain. Energy Rev.* 159 (2022), 112207, <https://doi.org/10.1016/j.rser.2022.112207>.
- [14] D.G. Atinafu, B.Y. Yun, S. Yang, H. Yuk, S. Wi, S. Kim, Structurally advanced hybrid support composite phase change materials: architectural synergy, *Energy Storage Mater.* 42 (2021) 164–184, <https://doi.org/10.1016/j.ensm.2021.07.022>.
- [15] L.T. Li, H.Z. Chen, Y.J. Shi, D. Xing, Human-body-temperature triggerable phase transition of W-VO₂@PEG nanoprobes with strong and switchable NIR-II absorption for deep and contrast-enhanced photoacoustic imaging, *ACS Nano* 16 (2) (2022) 2066–2076, <https://doi.org/10.1021/acsnano.1c07511>.
- [16] Y.Y. Xiao, D.Y. Bai, Z.P. Xie, Z.Y. Yang, J.H. Yang, X.D. Qi, Y. Wang, Flexible copper foam-based phase change materials with good stiffness-toughness balance, electro-to-thermal conversion ability and shape memory function for intelligent thermal management, *Compos. Part A-Appl. S.* 146 (2021), 106420, <https://doi.org/10.1016/j.compositesa.2021.106420>.
- [17] Y. Li, Y.Q. Li, X.B. Huang, H.Y. Zheng, G.L. Lu, Z.S. Xi, G. Wang, Graphene-CoO/PEG composite phase change materials with enhanced solar-to-thermal energy conversion and storage capacity, *Compos. Sci. Technol.* 195 (2020), 108197, <https://doi.org/10.1016/j.compscitech.2020.108197>.
- [18] S.B. Senturk, D. Kahraman, C. Alkan, I. Gokce, Biodegradable PEG/cellulose, PEG/agarose and PEG/chitosan blends as shape stabilized phase change materials for latent heat energy storage, *Carbohydr. Polym.* 84 (1) (2011) 141–144, <https://doi.org/10.1016/j.carbpol.2010.11.015>.
- [19] T.T. Qian, J.H. Li, X. Min, W.M. Guan, Y. Deng, L. Ning, Enhanced thermal conductivity of PEG/diatomite shape-stabilized phase change materials with Ag nanoparticles for thermal energy storage, *J. Mater. Chem. A* 3 (16) (2015) 8526–8536, <https://doi.org/10.1039/c5ta00309a>.
- [20] W. Aftab, A. Mahmood, W.H. Guo, M. Yousaf, H. Tabassum, X.Y. Huang, Z. B. Liang, A.Y. Cao, R.Q. Zou, Polyurethane-based flexible and conductive phase change composites for energy conversion and storage, *Energy Storage Mater.* 20 (2019) 401–409, <https://doi.org/10.1016/j.ensm.2018.10.014>.
- [21] M.Q. Wu, T.X. Li, P.F. Wang, S. Wu, R.Z. Wang, J. Lin, Dual-encapsulated highly conductive and liquid-free phase change composites enabled by polyurethane/graphite nanoplatelets hybrid networks for efficient energy storage and thermal management, *Small* 18 (9) (2022), 2105647, <https://doi.org/10.1002/smll.202105647>.
- [22] Q.H. Zhao, F.F. He, Q.P. Zhang, J.H. Fan, R. He, K. Zhang, H.J. Yan, W.B. Yang, Microencapsulated phase change materials based on graphene Pickering emulsion for light-to-thermal energy conversion and management, *Sol. Energy Mater. Sol. Cell.* 203 (2019), 110204, <https://doi.org/10.1016/j.solmat.2019.110204>.
- [23] A.N. Mustapha, Y. Zhang, Z.B. Zhang, Y.L. Ding, Y.L. Li, A systematic study on the reaction mechanisms for the microencapsulation of a volatile phase change material (PCM) via one-step in situ polymerisation, *Chem. Eng. Sci.* 252 (2022), 117497, <https://doi.org/10.1016/j.ces.2022.117497>.
- [24] P.K.S. Rathore, S.K. Shukla, N.K. Gupta, Potential of microencapsulated PCM for energy savings in buildings: a critical review, *Sustain. Cities Soc.* 53 (2020), 101884, <https://doi.org/10.1016/j.scs.2019.101884>.
- [25] X.T. Shi, M.R. Yazdani, R. Ajdary, O.J. Rojas, Leakage-proof microencapsulation of phase change materials by emulsification with acetylated cellulose nanofibrils, *Carbohydr. Polym.* 254 (2021), 117279, <https://doi.org/10.1016/j.carbpol.2020.117279>.
- [26] X. Yang, Y. Liu, Z.H. Lv, Q.X. Hua, L. Liu, B.M. Wang, J.W. Tang, Synthesis of high latent heat lauric acid/silica microcapsules by interfacial polymerization method for thermal energy storage, *J. Energy Storage* 33 (2021), 102059, <https://doi.org/10.1016/j.est.2020.102059>.
- [27] W.X. Luo, X.W. Hu, Y.H. Che, S. Zu, Q.L. Li, X.X. Jiang, D.J. Liu, Form-stable phase change materials enhanced photothermal conversion and thermal conductivity by Ag-expanded graphite, *J. Energy Storage* 52 (2022), 105060, <https://doi.org/10.1016/j.est.2022.105060>.
- [28] P. Cheng, X. Chen, H.Y. Gao, X.W. Zhang, Z.D. Tang, A. Li, G. Wang, Different dimensional nanoadditives for thermal conductivity enhancement of phase change materials: fundamentals and applications, *Nano Energy* 85 (2021), 105948, <https://doi.org/10.1016/j.nanoen.2021.105948>.
- [29] X.T. Shi, Y. Meng, R. Bi, Z.M. Wan, Y. Zhu, O.J. Rojas, Enabling unidirectional thermal conduction of wood-supported phase change material for photo-to-thermal energy conversion and heat regulation, *Compos. Part B-Eng.* 245 (2022), 110231, <https://doi.org/10.1016/j.compositesb.2022.110231>.
- [30] Y.H. Zhang, S.J. Park, In situ shear-induced mercapto group-activated graphite nanoplatelets for fabricating mechanically strong and thermally conductive elastomer composites for thermal management applications, *Compos. Part A-Appl. S.* 112 (2018) 40–48, <https://doi.org/10.1016/j.compositesa.2018.06.004>.
- [31] Y.H. Zhang, J.R. Choi, S.J. Park, Interlayer polymerization in amine-terminated macromolecular chain grafted expanded graphite for fabricating highly thermal conductive and physically strong thermoset composites for thermal management applications, *Compos. Part A-Appl. S.* 109 (2018) 498–506, <https://doi.org/10.1016/j.compositesa.2018.04.001>.
- [32] F. Zhang, D.H. Ren, Y.H. Zhang, L.Q. Huang, Y.X. Sun, W. Wang, Q. Zhang, W. Feng, Q.B. Zheng, Production of highly-oriented graphite monoliths with high thermal conductivity, *Chem. Eng. J.* 431 (2022), 134102, <https://doi.org/10.1016/j.cej.2021.134102>.
- [33] F. Zhang, C.B. Li, Y.H. Zhang, Y.X. Sun, X.M. Yao, L. Guo, J.Y. Wu, K. Dai, J.T. Wu, Q.B. Zheng, Facile preparation of large-scale expanded graphite/polydimethylsiloxane composites for highly-efficient electromagnetic interference shielding, *J. Mater. Chem. A* 10 (43) (2022) 23145–23154, <https://doi.org/10.1039/d2ta06263a>.
- [34] Y.H. Zhang, W. Wang, F. Zhang, L.Q. Huang, K. Dai, C.B. Li, D. Liu, Y.X. Sun, D. H. Ren, J.Y. Wu, Q.B. Zheng, Micro-diamond assisted bidirectional tuning of thermal conductivity in multifunctional graphene nanoplatelets/nanofibrillated cellulose films, *Carbon* 189 (2022) 265–275, <https://doi.org/10.1016/j.carbon.2021.12.067>.
- [35] Y. Zhang, Y.J. Heo, Y.R. Son, I. In, K.H. An, B.J. Kim, S.J. Park, Recent advanced thermal interfacial materials: a review of conducting mechanisms and parameters of carbon materials, *Carbon* 142 (2019) 445–460, <https://doi.org/10.1016/j.carbon.2018.10.077>.
- [36] F. Zhang, Y.Y. Feng, W. Feng, Three-dimensional interconnected networks for thermally conductive polymer composites: design, preparation, properties, and mechanisms, *Mat. Sci. Eng.-R* 142 (2020), 100580, <https://doi.org/10.1016/j.mser.2020.100580>.
- [37] X.W. Jia, Q.Y. Li, C.H. Ao, R. Hu, T. Xia, Z.H. Xue, Q.H. Wang, X.Y. Deng, W. Zhang, C.H. Lu, High thermal conductive shape-stabilized phase change materials of polyethylene glycol/boron nitride@chitosan composites for thermal energy storage, *Compos. Part A-Appl. S.* 129 (2020), 105710, <https://doi.org/10.1016/j.compositesa.2019.105710>.
- [38] G.Q. Yang, L.Y. Zhao, C.F. Shen, Z.P. Mao, H. Xu, X.L. Feng, B.J. Wang, X.F. Sui, Boron nitride microspheres bridged with reduced graphene oxide as scaffolds for multifunctional shape stabilized phase change materials, *Sol. Energy Mater. Sol. Cell.* 209 (2020), 110441, <https://doi.org/10.1016/j.solmat.2020.110441>.
- [39] M. Wu, T. Li, P. Wang, S. Wu, R. Wang, J. Lin, Dual-encapsulated highly conductive and liquid-free phase change composites enabled by polyurethane/graphite nanoplatelets hybrid networks for efficient energy storage and thermal management, *Small* 18 (9) (2021), <https://doi.org/10.1002/smll.202105647>.
- [40] J. Deng, X. Li, C. Li, T. Wang, R. Liang, S. Li, Q. Huang, G. Zhang, Multifunctional flexible composite phase change material with high anti-leakage and thermal conductivity performances for battery thermal management, *J. Energy Storage* 72 (2023), <https://doi.org/10.1016/j.est.2023.108313>.
- [41] X.F. Ran, H.R. Wang, Y.J. Zhong, F. Zhang, J. Lin, H. Zou, Z.M. Dai, B.L. An, Thermal properties of eutectic salts/ceramics/expanded graphite composite phase change materials for high-temperature thermal energy storage, *Sol. Energy Mater. Sol. Cell.* 225 (2021), 111047, <https://doi.org/10.1016/j.solmat.2021.111047>.
- [42] J. Yang, L.S. Tang, R.Y. Bao, L. Bai, Z.Y. Liu, W. Yang, B.H. Xie, M.B. Yang, An ice-templated assembly strategy to construct graphene oxide/boron nitride hybrid porous scaffolds in phase change materials with enhanced thermal conductivity and shape stability for light-thermal-electric energy conversion, *J. Mater. Chem. A* 4 (48) (2016) 18841–18851, <https://doi.org/10.1039/c6ta08454k>.
- [43] R.L. Wen, S.B. Zhu, M.M. Wu, W.X. Chen, Design and preparation of Ag modified expanded graphite based composite phase change materials with enhanced thermal conductivity and light-to-thermal properties, *J. Energy Storage* 41 (2021), 102936, <https://doi.org/10.1016/j.est.2021.102936>.

- [44] J.N. Shi, M.D. Ger, Y.M. Liu, Y.C. Fan, N.T. Wen, C.K. Lin, N.W. Pu, Improving the thermal conductivity and shape-stabilization of phase change materials using nanographite additives, *Carbon* 51 (2013) 365–372, <https://doi.org/10.1016/j.carbon.2012.08.068>.
- [45] X.W. Lin, X.L. Zhang, L. Liu, J.Y. Liang, W. Liu, Polymer/expanded graphite-based flexible phase change material with high thermal conductivity for battery thermal management, *J. Clean. Prod.* 331 (2022), 130014, <https://doi.org/10.1016/j.jclepro.2021.130014>.
- [46] X. Fang, L.W. Fan, Q. Ding, X. Wang, X.L. Yao, J.F. Hou, Z.T. Yu, G.H. Cheng, Y. C. Hu, K.F. Cen, Increased thermal conductivity of eicosane-based composite phase change materials in the presence of graphene nanoplatelets, *Energy Fuel*. 27 (7) (2013) 4041–4047, <https://doi.org/10.1021/ef400702a>.
- [47] Z.Y. Ling, J.J. Chen, T. Xu, X.M. Fang, X.N. Gao, Z.G. Zhang, Thermal conductivity of an organic phase change material/expanded graphite composite across the phase change temperature range and a novel thermal conductivity model, *Energy Convers. Manag.* 102 (2015) 202–208, <https://doi.org/10.1016/j.enconman.2014.11.040>.
- [48] S. Ganguli, A.K. Roy, D.P. Anderson, Improved thermal conductivity for chemically functionalized exfoliated graphite/epoxy composites, *Carbon* 46 (5) (2008) 806–817, <https://doi.org/10.1016/j.carbon.2008.02.008>.
- [49] Y.H. Zhang, Y. Fan, U. Kamran, S.J. Park, Improved thermal conductivity and mechanical property of mercapto group-activated boron nitride/elastomer composites for thermal management, *Compos. Part A-Appl. S.* 156 (2022), 106869, <https://doi.org/10.1016/j.compositesa.2022.106869>.
- [50] Y. Zhang, J.R. Choi, S.J. Park, Thermal conductivity and thermo-physical properties of nanodiamond-attached exfoliated hexagonal boron nitride/epoxy nanocomposites for microelectronics, *Compos. Part A-Appl. S.* 101 (2017) 227–236, <https://doi.org/10.1016/j.compositesa.2017.06.019>.
- [51] J.Y. Do, N. Son, J. Shin, R.K. Chava, S.W. Joo, M. Kang, n-Eicosane-Fe₃O₄@SiO₂@Cu microcapsule phase change material and its improved thermal conductivity and heat transfer performance, *Mater. Des.* 198 (2021), <https://doi.org/10.1016/j.matdes.2020.109357>.
- [52] Z.-j. Duan, H.-z. Zhang, L.-x. Sun, Z. Cao, F. Xu, Y.-j. Zou, H.-l. Chu, S.-j. Qiu, C.-l. Xiang, H.-y. Zhou, CaCl₂·6H₂O/Expanded graphite composite as form-stable phase change materials for thermal energy storage, *J. Therm. Anal. Calorim.* 115 (1) (2013) 111–117, <https://doi.org/10.1007/s10973-013-3311-0>.
- [53] E.C.B. Noyan, E. Onder, N. Sarier, R. Arat, Development of heat storing poly (acrylonitrile) nanofibers by coaxial electrospinning, *Thermochim. Acta* 662 (2018) 135–148, <https://doi.org/10.1016/j.tca.2018.02.008>.
- [54] A. Sari, T.A. Saleh, G. Hekimoğlu, V.V. Tyagi, R.K. Sharma, Microencapsulated heptadecane with calcium carbonate as thermal conductivity-enhanced phase change material for thermal energy storage, *J. Mol. Liq.* 328 (2021), <https://doi.org/10.1016/j.molliq.2021.115508>.
- [55] S. Song, T. Zhao, W. Zhu, F. Qiu, Y. Wang, L. Dong, Natural microtubule-encapsulated phase-change material with simultaneously high latent heat capacity and enhanced thermal conductivity, *ACS Appl. Mater. Interfaces* 11 (23) (2019) 20828–20837, <https://doi.org/10.1021/acsami.9b04523>.
- [56] Y. Guo, C.C. Dun, J.W. Xu, J.K. Mu, P.Y. Li, L.W. Gu, C.Y. Hou, C.A. Hewitt, Q. H. Zhang, Y.G. Li, D.L. Carroll, H.Z. Wang, Ultrathin, washable, and large-area graphene papers for personal thermal management, *Small* 13 (44) (2017) 1702645, <https://doi.org/10.1002/sml.201702645>.
- [57] X. Zhao, L.Y. Wang, C.Y. Tang, X.J. Zha, Y. Liu, B.H. Su, K. Ke, R.Y. Bao, M.B. Yang, W. Yang, Smart Ti₃C₂T_x MXene fabric with fast humidity response and Joule heating for healthcare and medical therapy applications, *ACS Nano* 14 (7) (2020) 8793–8805, <https://doi.org/10.1021/acsnano.0c03391>.
- [58] Q.W. Wang, H.B. Zhang, J. Liu, S. Zhao, X. Xie, L.X. Liu, R. Yang, N. Koratkar, Z. Z. Yu, Multifunctional and water-resistant MXene-decorated polyester textiles with outstanding electromagnetic interference shielding and Joule heating performances, *Adv. Funct. Mater.* 29 (7) (2019), 1806819, <https://doi.org/10.1002/adfm.201806819>.
- [59] L. Li, Y.X. Cao, X.Y. Liu, J.F. Wang, Y.Y. Yang, W.J. Wang, Multifunctional MXene-based fireproof electromagnetic shielding films with exceptional anisotropic heat dissipation capability and Joule heating performance, *ACS Appl. Mater. Interfaces* 12 (24) (2020) 27350–27360, <https://doi.org/10.1021/acscami.0c05692>.
- [60] X. Guo, C. Liu, N. Li, S. Zhang, Z. Wang, Electrothermal conversion phase change composites: the case of polyethylene glycol infiltrated graphene oxide/carbon nanotube networks, *Ind. Eng. Chem. Res.* 57 (46) (2018) 15697–15702.
- [61] Z.L. Ma, S.L. Kang, J.Z. Ma, L. Shao, Y.L. Zhang, C. Liu, A.J. Wei, X.L. Xiang, L. F. Wei, J.W. Gu, Ultraflexible and mechanically strong double-layered aramid nanofiber-Ti₃C₂T_x MXene/silver nanowire nanocomposite papers for high-performance electromagnetic interference shielding, *ACS Nano* 14 (7) (2020) 8368–8382, <https://doi.org/10.1021/acsnano.0c02401>.
- [62] H.K. Choi, A. Lee, M. Park, D.S. Lee, S. Bae, S.K. Lee, S.H. Lee, T. Lee, T.W. Kim, Hierarchical porous film with layer-by-layer assembly of 2D copper nanosheets for ultimate electromagnetic interference shielding, *ACS Nano* 15 (1) (2021) 829–839, <https://doi.org/10.1021/acsnano.0c07352>.
- [63] J.H. Lee, Y.S. Kim, H.J. Ru, S.Y. Lee, S.J. Park, Highly flexible fabrics/epoxy composites with hybrid carbon nanofillers for absorption-dominated electromagnetic interference shielding, *Nano-Micro Lett.* 14 (1) (2022) 188, <https://doi.org/10.1007/s40820-022-00926-1>.
- [64] L. Sun, Y. Yang, H. Ni, D. Liu, Z. Sun, P. Li, J. Yu, Enhancement of CO₂ adsorption performance on hydrotalcites impregnated with alkali metal nitrate salts and carbonate salts, *Ind. Eng. Chem. Res.* 59 (13) (2020) 6043–6052, <https://doi.org/10.1021/acs.iecr.9b05700>.
- [65] X.G. Yang, T. Liu, Y. Gao, S.H. Ge, Y.J. Leng, D.H. Wang, C.Y. Wang, Asymmetric temperature modulation for extreme fast charging of lithium-ion batteries, *Joule* 3 (12) (2019) 3002–3019, <https://doi.org/10.1016/j.joule.2019.09.021>.
- [66] C.Y. Wang, G.S. Zhang, S.H. Ge, T. Xu, Y. Ji, X.G. Yang, Y.J. Leng, Lithium-ion battery structure that self-heats at low temperatures, *Nature* 529 (7587) (2016) 515–518, <https://doi.org/10.1038/nature16502>.